P35 **TROCHOIDAL PATHS TRACED OUT BY A SUBVORTEX REVOLVING AROUND A PARENT VORTEX: A SIMULATION STUDY**

Vincent T. Wood *
NOAA/OAR/National Severe Storms Laboratory, Norman, Oklahoma, USA

1. INTRODUCTION

Trochoidal tracks traced out by tornadoes revolving around parent mesocyclones (Fig. 1) have been documented by Fujita (1963), Agee et al. (1976; 1977), Brown and Knupp (1980), Bluestein (1983), Wakimoto and Atkins (1996), Wurman and Gill (2000), Wakimoto et al. (2003) among others. Based on a dual-Doppler radar analysis, Ray et al. (1976) showed that location of the Harrah, Oklahoma tornado of 8 June 1974 with respect to a parent circulation was consonant with the veering of the damage path to the right of storm motion. Tornado revolution about parent mesocyclone center is analogous to multiple vortices revolving about a parent tornado center (Fujita et al. 1970; Fujita 1981; Forbes and Bluestein 2001). As documented by damage surveys, photographs and mobile Doppler radar data, a loop was executed as the Moore, Oklahoma tornado of 20 May 2013 revolved cyclonically around a supercell, low-level mesocyclone circulation once in the vicinity of the Moore Medical Center (Atkins et al. 2014; Burgess et al. 2014; Kurdzo et al. 2015). Wakimoto et al. (2015, 2016) surveyed the El Reno, Oklahoma tornado damage path of 31 May 2013, revealing that the tornado with several embedded intense multiple-vortices moved rapidly in complex trochoidal/cycloidal/looping tracks while turning left slowly (Fig. 2).

Suction marks are the most interesting and useful of the marks left by tornadoes crossing open fields (Fujita et al. 1970). Fujita et al. originally developed a trochoidal hypothesis in which simple parametric equations of a trochoid were taken with an x-axis along the path of a tornado. They computed varying ratios of a subvortex's circular motion to a parent tornado's rectilinear motion to produce various shapes of a subvortex's trochoidal marks, loop widths and shifts. If the Fujita et al. technique were applied to tornado revolution around a parent mesocyclone axis, the utility of the technique was limited because the circular and rectilinear motions were assumed to be constant. For example, the trochoid hypothesis did not account for a left- or right-turning or rectilinear parent tornado movements at various speeds, whereas the multiple vortices' axes revolving about the parent tornado axis maintained constant circular motions. The lack of such information motivated the author to extend the Fujita et al. technique by which the subvortex's revolution speed, the parent vortex's translational velocity and direction toward which the parent vortex travels are considered as non-uniform.

The objective of the paper is to develop novel parametric equations for investigating and elucidating the transient behaviors of tracks traced out by a hypothetical subvortex revolving around a hypothetical parent vortex. These equations express a set of quantities as explicit functions of independent variables. The following variables characterize different types of sub-vortex tracks: (a) translational speed of the parent vortex, (b) direction toward which the vortex travels in a rectilinear or curvilinear path, (c) beginning time at which a subvortex track commences, (d) ending time of the track, (e) speed at which the subvortex is revolving cyclonically around the parent vortex axis, (f) radial distance of subvortex axis from parent vortex axis, and (g) linear and nonlinear parent vortex path lengths and subvortex damage path lengths. The evolutionary characteristics of several parameters were plotted against time to interpret the transient behaviors of simulated tracks that bear resemblance to the observed tornado damage tracks.

* *Corresponding author address:* Vincent T. Wood, National Severe Storms Laboratory, 120 David L. Boren Blvd., Norman, Oklahoma 73072, USA; e-mail: Vincent.Wood@noaa.gov

2. KINEMATICS OF A TROCHOIDAL MOTION

On a two-dimensional, horizontal plane, we consider the positions of a parent vortex center at two different times t and $t+\Delta t$, where Δt is a small increment time (Fig. 3). The position relative to a given reference frame with origin O is given by the position vector $\mathbf{R}_{pv}$ from the origin to point P_{pv}. The subscript pv represents *p*arent *v*ortex. If the parent vortex center P_{pv} is in motion relative to the reference frame, the position vector $\mathbf{R}_{pv}$ is a function of time t, and can be expressed as $\mathbf{R}_{pv} = \mathbf{R}_{pv}(t)$. Considering an infinitesimal time increment ($\Delta t \to 0$), the vector translational velocity $\mathbf{C}_{pv}(t)$ of the parent vortex axis at $P_{pv}(t)$ relative to the reference frame at time t is defined by

$$\lim_{\Delta t\to 0}\frac{\mathbf{R}_{pv}(t+\Delta t)-\mathbf{R}_{pv}(t)}{\Delta t}=\lim_{\Delta t\to 0}\frac{\Delta\mathbf{R}_{pv}}{\Delta t}=\frac{d\mathbf{R}_{pv}(t)}{dt}=\mathbf{C}_{pv}(t)\,, (1)$$

where the vector $\mathbf{R}_{pv}(t+\Delta t)-\mathbf{R}_{pv}(t)=\Delta\mathbf{R}_{pv}$ is the change in position of the parent vortex axis, or displacement of $P_{pv}(t+\Delta t)$ during the infinitesimal interval of time Δt. The parent vortex's velocity $C_{pv}(t)$ is the rate of change of the position of the parent vortex axis between points $P(t)$ and $P(t+\Delta t)$. The magnitude of the velocity vector $\mathbf{C}_{pv}(t) = C_{pv}(t)\,\mathbf{e}_{Dir_{pv}}$ is the parent vortex's translational speed $C_{pv}(t) = |\mathbf{C}_{pv}(t)|$; the vortex can accelerate, decelerate or maintain its constant speed with time. The unit vector $\mathbf{e}_{Dir_{pv}} = \sin[Dir_{pv}(t)]\,\mathbf{i} + \cos[Dir_{pv}(t)]\,\mathbf{j}$ is tangent to the parent vortex's translational direction $Dir_{pv}(t)$ $[=\frac{\pi}{2}-\theta_{pv}(t)]$ toward which the vortex moves, and is measured clockwise from due north. The term $\theta_{pv}(t)[=\frac{\pi}{2}-Dir_{pv}(t)]$ is the angle between the $\mathbf{e}_{Dir_{pv}}$ vector and the x-axis is measured counterclockwise from due east (Fig. 3). The point

$P_{pv}(t+\Delta t)$ lies on the desired line if and only if $\mathbf{R}_{pv}(t+\Delta t)-\mathbf{R}_{pv}(t)$ is parallel to $\mathbf{C}_{pv}(t)$. A new vector (red) is parallel to $\mathbf{C}_{pv}(t)$ if and only if it equals some scalar multiple of $\mathbf{C}_{pv}(t)$, so that the condition that $P_{pv}(t+\Delta t)$ be on the line is that

$$\mathbf{R}_{pv}(t+\Delta t)-\mathbf{R}_{pv}(t)=\Delta\mathbf{R}_{pv}=\Delta t\,\mathbf{C}_{pv}(t)\ , \quad (2)$$

for some time interval Δt of duration. Note that $\mathbf{R}_{pv}(t+\Delta t)-\mathbf{R}_{pv}(t)=\Delta\mathbf{R}_{pv}$ is equivalent to $\Delta t\,\mathbf{C}_{pv}(t)$. The parent vortex can move in a rectilinear line or turn left or right in a curvilinear path (blue dotted curve). The position and velocity of the parent vortex can be specified only relative to the reference frame.

A subvortex revolves at its angular velocity $\Omega_{sv}(t)$ cyclonically around the parent vortex axis. $\Omega_{sv}(t)$ is the revolution angular velocity of the line (position vector) from the axis of the parent vortex $P_{pv}(t)$ to the subvortex axis (Fig. 4) as a function of time. The angular velocity may increase, maintain, or decrease its speed. Therefore, the position vector has a magnitude equal to the radial distance, and a direction determined by $\mathbf{e}_r$ (Fig. 4). It is given by

$$\mathbf{D}_{sv}(t)=D_{sv}(t)\,\mathbf{e}_r, \quad (3)$$

where $D_{sv}(t)$ is the radial distance from the parent vortex axis to the subvortex tracing out the damage path at t, and the subscript in $D_{sv}(t)$ represents subvortex. The unit vector $\mathbf{e}_r=\cos\left[\Omega_{sv}(t)\times t+\theta_{sv}+\theta_{pv}(t)\right]\mathbf{i}+\sin\left[\Omega_{sv}(t)\times t+\theta_{sv}+\theta_{pv}(t)\right]\mathbf{j}$ is directed away from $P_{pv}(t)$. θ_{sv} is the angle of the subvortex's initial position ($t=0$) relative to the orientation of the parent vortex's track, measured in a counterclockwise direction. $D_{sv}(t)$ decreases, increases or remains unchanged with time, while at the same time, the subvortex revolves cyclonically about the parent vortex axis.

A novel equation of a trochoidal track is written in vector form by adding $\mathbf{D}_{sv}(t)$ to Eq. (2) and replacing the subscript pv by tro in $\mathbf{R}_{pv}$. It is given by

$$\mathbf{R}_{tro}(t+\Delta t)=\mathbf{R}_{tro}(t)+\Delta t\,\mathbf{C}_{pv}(t)+\mathbf{D}_{sv}(t),\qquad t_b\le t\le t_e\ , \quad (4)$$

where $\mathbf{R}_{tro}(t+\Delta t)$ represents the discrete position vector of the subvortex's track at future time $t+\Delta t$. The subscript in $\mathbf{R}_{tro}$ represents the trochoid traced out by the subvortex axis [representing $D_{sv}(t)$] as it revolves about the axis of the translating parent vortex. $\mathbf{R}_{tro}(t)$ is the position vector of the trochoidal track at instant time t and is ground-relative. t_b is the beginning time at which a damage track commences; t_e is the ending time of the track. The varying time $t=(i-1)\Delta t$ is measured from t_b to t_e, with the time interval Δt and its index $1\le i\le\left(\frac{t_e-t_b}{\Delta t}\right)+1$.

Using a Lagrangian specification of the track field, Eq. (4) are written in scalar forms

$$\begin{aligned}X_{tro}(t+\Delta t)&=X_{tro}(t)+\Delta t\,C_{pv}(t)\,\sin[Dir_{pv}(t)]\\&\quad+D_{sv}(t)\cos[\Omega_{sv}(t)\times t+\theta_{sv}+\theta_{pv}(t)]\ ,\\Y_{tro}(t+\Delta t)&=Y_{tro}(t)+\Delta t\,C_{pv}(t)\,\cos[Dir_{pv}(t)]\\&\quad+D_{sv}(t)\sin[\Omega_{sv}(t)\times t+\theta_{sv}+\theta_{pv}(t)]\ ,\end{aligned}\quad (5)$$

where X_{tro} and Y_{tro}, respectively, are the eastward and northward Cartesian components of the position track vector $\mathbf{R}_{tro}$.

Differentiating Eq. (4) with respect to time *t* yields the vector trochoidal velocity $\mathbf{C}_{tro}(t)=U_{tro}(t)\,\mathbf{i}+V_{tro}(t)\,\mathbf{j}$, given as

$$\mathbf{C}_{tro}(t)=\frac{d\mathbf{R}_{tro}(t)}{dt}=\mathbf{C}_{pv}(t)+\Delta t\frac{d\mathbf{C}_{pv}(t)}{dt}+\mathbf{C}_{sv}(t)\ , \quad (6)$$

where $U_{tro}(t)$ and $V_{tro}(t)$ are the positive Cartesian horizontal components of $\mathbf{C}_{tro}(t)$ directed eastward and northward, respectively. Here, the magnitude of $|\mathbf{C}_{tro}(t)|$ is the subvortex's ground-relative, trochoidal speed, expressed by,

$$C_{tro}(t)=|\mathbf{C}_{tro}(t)|=\sqrt{U_{tro}^2(t)+V_{tro}^2(t)}\ , \quad (7)$$

and

$$\frac{d\mathbf{C}_{pv}(t)}{dt}=\frac{dC_{pv}(t)}{dt}\,\mathbf{e}_{Dir_{pv}}+C_{pv}(t)\,\frac{d\mathbf{e}_{Dir_{pv}}}{dt} \quad (8)$$

is the change in velocity and translational direction of the parent vortex axis, respectively. The second term $\frac{d\mathbf{e}_{Dir_{pv}}}{dt}$ on the right-hand side of Eq. (8) is given by

$$\frac{d\mathbf{e}_{Dir_{pv}}}{dt}=\frac{dDir_{pv}(t)}{dt}\left\{\cos\left[Dir_{pv}(t)\right]\mathbf{i}-\sin\left[Dir_{pv}(t)\right]\mathbf{j}\right\}. \quad (9)$$

The unit vector $\frac{d\mathbf{e}_{Dir_{pv}}}{dt}$ is perpendicular to $\mathbf{e}_{Dir_{pv}}$ and points in the direction of increasing the parent vortex's translational direction $Dir_{pv}(t)$ (measured clockwise from due north). The trochoidal direction toward which the subvortex moves along the trochoidal track is represented by $Dir_{tro}(t)=\tan^{-1}[U_{tro}(t)/V_{tro}(t)]$, and is measured clockwise from due north. The scalar forms of Eq. (6) will be shown subsequently.

The last term on the right-hand side of Eq. (6) represents a subvortex's velocity vector $\mathbf{C}_{sv}(t)$ on the circumference of the circle having its radius $D_{sv}(t)$ and is given by, with the aid of Eq. (3),

$$\mathbf{C}_{sv}(t)=\frac{d\mathbf{D}_{sv}(t)}{dt}=C_{sv\_r}(t)\,\mathbf{e}_r+C_{sv\_t}(t)\,\mathbf{e}_t\ . \quad (10)$$

$\mathbf{C}_{sv}(t)$ may be partitioned into (a) the radial component $C_{sv\_r}(t)\,\mathbf{e}_r$ that is the rate at which $\mathbf{D}_{sv}(t)$ stretches or shrinks with time in the $\mathbf{e}_r$ direction (Fig. 4), and is given by

$$C_{sv\_r}(t)=\frac{dD_{sv}(t)}{dt}\ , \quad (11)$$

where $C_{sv\_r}(t)$ is the radial velocity component, and (b) the tangential component $C_{sv\_t}(t)\,\mathbf{e}_t$ that is the rate at which the subvortex axis revolves with time around the circumference of the circle having radius $D_{sv}(t)$ in the $\mathbf{e}_t$ direction, and is expressed by

$$C_{sv\_t}(t) = \left[\Omega_{sv}(t) + t\frac{d\Omega_{sv}(t)}{dt} + \frac{d\theta_{pv}(t)}{dt}\right] D_{sv}(t) \text{ , (12)}$$

where $C_{sv\_t}(t)$ is the circumferential (or tangential) velocity component. The $d\theta_{pv}(t)/dt$ term represents the curvature of the parent vortex's path from $P_{pv}(t)$ to $P_{pv}(t+\Delta t)$. The curvature may be small comparing to $\Omega_{sv}(t)$. If the vortex travels in a rectilinear motion with time t, $d\theta_{pv}(t)/dt$ equals zero. The unit vector $\mathbf{e}_t$ is perpendicular to $\mathbf{e}_r$ and points in the direction of increasing the angle $[\Omega_{sv}(t) \times t + \theta_{sv} + \theta_{pv}(t)]$, given by $\mathbf{e}_t = -\sin[\Omega_{sv}(t) \times t + \theta_{sv} + \theta_{pv}(t)]\,\mathbf{i} + \cos[\Omega_{sv}(t) \times t + \theta_{sv} + \theta_{pv}(t)]\,\mathbf{j}$. Note that the unit vectors $\mathbf{e}_r$ and $\mathbf{e}_t$ are related to the Cartesian unit vectors $\mathbf{i}$ and $\mathbf{j}$. This expresses the subvortex axis's revolution speed magnitude $|\mathbf{C}_{sv}(t)|$ as the sum of a radial component, directed away from or towards the parent vortex axis with magnitude $C_{sv\_r}(t)$, and a tangential component with magnitude $C_{sv\_t}(t)$. Note that $|\mathbf{C}_{sv}(t)|$ may be expressed as

$$C_{sv}(t) = |\mathbf{C}_{sv}(t)| = \sqrt{C_{sv\_r}^2(t) + C_{sv\_t}^2(t)} \text{ .} \quad (13)$$

If $D_{sv}(t)$ is constant with time, $C_{sv\_t}(t)$ in Eq. (11) is zero, indicating that the subvortex axis is rotating in a circular motion at its constant revolution speed $C_{sv\_t}(t)$ without stretching or shrinking $D_{sv}(t)$ in the $\mathbf{e}_r$ direction. When $C_{sv\_t}(t)$ is zero, the subvortex is located at the center of the parent vortex, because $D_{sv}(t)$ is zero in Eq. (12).

Fujita et al. (1970, their Fig. 84) and Wakimoto et al. (2003) created an idealized illustration of basic trochoidal marks as a function of (a) the revolution speed $|\mathbf{C}_{sv}(t)|$ of a hypothetical subvortex axis around a parent vortex axis and (b) the translational speed $|\mathbf{C}_{pv}(t)|$ of the parent vortex center (Fig. 1). If one thinks of the subvortex path as being traced out by flow around the translational parent vortex, then $dY_{tro}(t)/dt$ and $dX_{tro}(t)/dt$ are, respectively, the northward and eastward trochoidal velocity components, as viewed from top, and are given by

$$\frac{dY_{tro}(t)}{dX_{tro}(t)} = \frac{dY_{tro}(t)/dt}{dX_{tro}(t)/dt} = \frac{V_{tro}(t)}{U_{tro}(t)} \text{ ,} \quad (14)$$

where the scalar forms of Eq. (6) are given by

$$\begin{aligned} U_{tro}(t) = \frac{dX_{tro}(t)}{dt} &= [C_{pv}(t) + \Delta t\frac{dC_{pv}(t)}{dt}]\sin[Dir_{pv}(t)] \\ &+\Delta t\frac{dDir_{pv}(t)}{dt}C_{pv}(t)\cos[Dir_{pv}(t)] \\ &+C_{sv\_r}(t)\cos[\Omega_{sv}(t)\times t + \theta_{sv} + \theta_{pv}(t)] \\ &-C_{sv\_t}(t)\sin[\Omega_{sv}(t)\times t + \theta_{sv} + \theta_{pv}(t)] \text{ ,} \quad (15a) \\ V_{tro}(t) = \frac{dY_{tro}(t)}{dt} &= [C_{pv}(t) + \Delta t\frac{dC_{pv}(t)}{dt}]\cos[Dir_{pv}(t)] \\ &-\Delta t\frac{dDir_{pv}(t)}{dt}C_{pv}(t)\sin[Dir_{pv}(t)] \\ &+C_{sv\_r}(t)\sin[\Omega_{sv}(t)\times t + \theta_{sv} + \theta_{pv}(t)] \\ &+C_{sv\_t}(t)\cos[\Omega_{sv}(t)\times t + \theta_{sv} + \theta_{pv}(t)] \text{ .} \quad (15b) \end{aligned}$$

Eq. (14) enables one to find the slope $dY_{tro}(t)/dX_{tro}(t)$ of the tangent to a parametric curve. It can been seen from the equation that the curve has a horizontal tangent (eastward) when $dY_{tro}(t)/dt$ = 0, provided that $dX_{tro}(t)/dt \neq 0$. Furthemore, the curve has a vertical tangent (northward) when $dX_{tro}(t)/dt$ = 0, provided that $dY_{tro}(t)/dt \neq 0$.

For the sake of simplicity, we consider the path of a parent vortex center to be along the x-axis when we assume that $Dir_{pv}(t)$, $\theta_{pv}(t)$, and $D_{sv}(t)$ are constant with time so that Eq. (14), via the aid of Eq. (15), is simplified to

$$\frac{V_{tro}(t)}{U_{tro}(t)} = \frac{R\cos[\Omega_{sv}(t)\times t + \theta_{sv}]}{1 - R\sin[\Omega_{sv}(t)\times t + \theta_{sv}]} \text{ ,} \quad (16)$$

where $R[\equiv C_{sv\_t}(t)/C_{pv}(t)]$ is the ratio of the subvortex's revolution speed $C_{sv\_t}(t)$ $[= \Omega_{sv}(t)D_{sv}(t)]$ to the parent vortex's translational speed $C_{pv}(t)$, $C_{sv\_r}(t) = 0$, $Dir_{pv}(t)$ = 90°, and $\theta_{pv}(t)$ = 0°. When $R = 1$, the trochoidal mark is *cycloidal*, representing a sharply-peaked track similar to the pointed trochoid that is produced when $C_{sv\_\tau}(t)$ is equal to $C_{pv}(t)$. When $R > 1$, a loop results. A broadly-peaked track is produced when $R < 1$. Note that Eq. (16) is analogous to Eq. (10) of Fujita et al. (1970).

From elementary calculus, if a curve is described by the parametric equations $x = f(t)$, $y = g(t)$, where df/dt and dg/dt are continuous on $[\alpha, \beta]$ and the curve is traversed exactly once as t increases from α to β, then the arc length of the curve is given by

$$L = \int_\alpha^\beta \sqrt{\left(\frac{dx}{d\tau}\right)^2 + \left(\frac{dy}{d\tau}\right)^2}\, d\tau \text{ , } \alpha \leq t \leq \beta \text{ ,} \quad (17)$$

where τ is a dummy variable for the integration. Replacing x by X_{tro} and y by Y_{tro} and then substituting U_{tro} into dX_{tro}/dt and V_{tro} into dY_{tro}/dt in Eq. (17) yields a subvortex's damage path length PL_{tro},

$$PL_{tro} = \int_{t_b}^{t_e} \sqrt{U_{tro}^2(\tau) + V_{tro}^2(\tau)}\, d\tau = \int_{t_b}^{t_e} C_{tro}(\tau)\, d\tau \text{ .} \quad (18)$$

Furthermore, the path length (PL_{pv}) of a parent vortex can be obtained in an analogous manner to the development of Eq. (18), given by

$$PL_{pv} = \int_{t_b}^{t_e} C_{pv}(\tau)\, d\tau \text{ .} \quad (19)$$

Eq. (19) is valid for varying $C_{pv}(t)$. If $C_{pv}(t)$ is constant with time, then the equation is simplified to $PL_{pv} = C_{pv}(t_e - t_b)$, regardless of a rectilinear or curvilinear path.

Following the approach of Fujita et al. (1970) and Agee et al. (1976), the time difference ($\Delta\tau$) between two successive points of zero or vertical slope of a trochoidal curve may be expressed by

$$\Delta\tau = \tau_2 - \tau_1 = \frac{2\pi}{\Omega_{sv}} \text{ ,} \quad (20)$$

where τ_1 and τ_2, respectively, are the times of the first and second points; and Ω_{sv} is assumed to be constant between the two points.

3. SIMULATION RESULTS

This section uses Eqs. (3)-(20) to provide what each input parameter may be able to deduce about the transient behaviors of trochoidal marks traced out by a hypothetical subvortex revolving around a hypothetical parent vortex. Table 1 lists the selected input parameter values for simulating a model tornado axis revolving cyclonically around a model mesocyclone axis in six experiments. The tornado axis is assumed to be vertical, although mobile, phased-array, Doppler radar observations of tilted tornadic vortex signatures with height were documented by French et al. (2014). To represent some of the variety found in nature, we assume the mesocyclone having a maximum tangential velocity of 25 m s^{-1} at a radius of 2.5 km. To simulate the tornado axis revolving cyclonically around the mesocyclone axis, $D_{sv}(t)$ is assumed to be 1.5 km, and the angular velocity $\Omega_{sv}(t)$ is assumed to be 0.01 s^{-1} for all times. Thus, $C_{sv\_t}(t)$ is 15 m s^{-1}, which is the tangential component of speed of the tornado axis on the circumference of the circle (e.g., Fig. 4) having a radius $D_{sv}(t)$. The duration of the mesocyclone is 30 min.

3.1 Experiment A

Figure 5 presents an idealized illustration of basic trochoidal mark as a function of $R[\equiv C_{sv\_t}(t)/C_{pv}(t)]$. We consider the problem of a mesocyclone moving eastward [$Dir_{pv}(t) = 90°$] with a constant $C_{pv}(t)$ of 25 m s^{-1} in a rectilinear motion. A tornado revolved cyclonically at a constant $C_{sv\_t}(t)$ value of 15 m s^{-1} around the mesocyclone center. This value was calculated from Eq. (12). At $t_b = 0$ min, a damage track commenced at $x = 0.0$ km and $y = $ -1.5 km; the track at $x = 43.8$ km and $y = $ -1.0 km ended at $t_e = 30$ min. Table 1 lists the selected parameters for experiment A.

As shown in the upper-right corner of Fig. 5b, a small time increment (Δt) of 10 s is used to illustrate a distance between two red dots. Two blue dots along the red dotted curve represent the 1-min update of the Phased Array Radar (PAR). At the same time, two black dots along the curve refer to a 5-min update of the Weather Surveillance Radar-1988 (WSR-88D). The PAR's lowest elevation angle of 0.5° was revisited every 1 min or less (Heinselman et al. 2008). High temporal resolution volumetric radar data are a necessity for rapid identification and confirmation of weather phenomena including tornadic vortex signatures within parent mesocyclone vortex signatures (Brown et al. 1978) that can develop within minutes.

The red dotted curve represents a trochoidal track traced out by the tornado axis on a radius (representing D_{sv}, green line) of a gray, interior circle inside a gray, exterior circle (representing a propagating mesocyclone) as the interior circle rolls. The salient feature of Figs. 5a and 5b is the trochoidal mark with broadly-peaked ridges associated with greater curvature and flatter troughs associated with lesser curvature. This is owing to the fact that the parent mesocyclone's translational speed $C_{pv}(t)$ is greater than the tornado's revolution speed $C_{sv\_t}(t)$, thus yielding $R < 1.0 = R_{cyc}$ (indicated by gray horizontal dashed line in Fig. 5c). Note that a blue circled line representing $R < 1.0$ is shown below the R_{cyc} line.

The evolutionary characteristics of the tornado's trochoidal speed $C_{tro}(t)$ and trochoidal direction $Dir_{tro}(t)$, tornado revolution direction $Dir_{sv}(t)$, and damage path length PL_{tro} as well as the mesocyclone's translational speed $C_{pv}(t)$, translational direction $Dir_{pv}(t)$, and path length PL_{pv} are illustrated in Fig. 5c. The green $Dir_{sv}(t)$ line centered at the interior circle is rotating cyclonically as the mesocyclone is propagating eastward. To the left (right) of the mesocyclone rectilinear track, the closer (farther apart) two red dots, the slower (faster) the trochoidal speeds $C_{tro}(t)$, as indicated by the green, converging (diverging) $D_{sv}(t)$ lines, (Figs. 5a and 5b). A black dashed line representing $C_{pv}(t)$ passes through a red, wavy curve represented by $C_{tro}(t)$. Between $t = 3$ min and $t = 7.5$ min, $C_{tro}(t) \leq C_{pv}(t)$, suggestive of the fact that the tornado's curvilinear motion is slower than the mesocyclone's rectilinear motion. Also, $C_{tro}(t) \geq C_{pv}(t)$ occurs between $t = 7.5$ min and $t = 13.5$ min, indicating that the tornado's center in its curvilinear path moves faster than the rectilinear motion of the mesocyclone. The interpretation of the $C_{tro}(t)$ curve shown in Fig. 5c is straightforward, because Fig. 1 does not tell us how the tornado's trochoidal speed $C_{tro}(t)$ along the trochoidal mark varies with time. Note that the profile of $Dir_{tro}(t)$ is nonlinear.

The tornado's damage path length (PL_{tro}), as calculated from Eq. (18), is 48 km, which is slightly longer than the mesocyclone's path length (PL_{pv}) of 45 km computed from Eq. (19). From Eq. (20), $\Delta\tau$ is found to be 628 s (~10.5 min), which favorably concur with the time difference between the first and second broadly-peak ridges as well as between the first and second flatter troughs.

3.2 Experiment B

In Experiment A, we demonstrated that the ratio of $C_{sv\_t}(t)/C_{pv}(t) < 1.0$ can affect the transient behaviors of simulated trochoidal tracks. Now, we conduct another experiment (Exp B) using $R = 1.0$. In Table 1 and Fig. 6, we decrease $C_{pv}(t)$ to 15 m s^{-1} to match $C_{sv\_t}(t)$, while other parameters remain unchanged. The simulated damage track of the model tornado shows a trochoidal mark that has approached a cycloid with a zero-angle cusp (vertical slope) for a crest (Figs. 6a and 6b). Three significant track shifts occurred at three cycloids, wherein the mark with the cusp-shaped crests was produced when $R = 1.0 = R_{cyc}$, as shown by the blue circled line overlaid on the gray dashed line in Fig. 6c. This figure provides the evolutionary characteristics of the tornado's trochoidal motion. The prominent feature of Fig. 6 is that the minimum value of $C_{tro}(t)$ locally was zero (maximum value) to the left (right) of the mesocyclone track. This is indicative of the fact that the tornado situated to the left of the mesocyclone path was stationary possibly for a long duration. The tornado began its speedup as it revolved behind the mesocyclone center. To the right of the mesocyclone track, the tornado rapidly approached until it reached its maximum at 30 m s^{-1}. The tornado then started its slowdown as it continued to revolve in front of the mesocyclone center. The second prominent feature is that the tornado's $Dir_{tro}(t)$ no longer changed nonlinearly, like it did in Fig. 5, as the tornado revolved around the mesocyclone center. As the tornado progressively approached from northeast toward north, it slowed down to zero. Then, the tornado abruptly changed its direction from north to south, before resuming a more normal eastward motion.

The third prominent feature is that the tornado's damage path length (PL_{tro}) was much longer than the mesocyclone's path length (PL_{pv}) when the mesocyclone's decreased $C_{pv}(t)$ was equal to the tornado's constant $C_{sv\_t}(t)$ than when $C_{pv}(t)$ was greater than $C_{sv\_t}(t)$ as in Fig. 5. At the end of 30 min, both PL_{tro} and PL_{pv} in association with $R = 1.0$ were shorter than those in association with $R < 1.0$, as comparison between Fig. 5c and Fig. 6c illustrates. Furthermore, the distance between two successive crested ridges or flatter troughs decreased with increasing R, while at the same time, $\Delta\tau$ was again found to be 10.5 min. It is indicative that $\Delta\tau$ is independent of R, as shown by Eq. (20).

3.3 Experiment C

What would happen to the tornado's trochoidal speed $C_{tro}(t)$ and direction $Dir_{tro}(t)$ when $C_{pv}(t)$ is further decreased to less than $C_{sv\_t}(t)$, while other parameters remain constant (Table 1)? The evolutionary characteristics of several parameters plotted against time to interpret the transient behaviors of simulated tracks are presented in Fig. 7.

Since $R > 1.0$, three prominent loops were produced during a 30-min mesocyclone track (Fig. 7b). This was because the tornado revolution around the mesocyclone center was faster than the slow-propagating mesocyclone, as expected. The tornado's damage path length (PL_{tro}) was 27 km, which was much longer than that of the mesocyclone ($PL_{pv} = 9$ km), as indicated by green and gray solid curves in Fig. 7c, respectively. Each loop's area increased with increasing R.

The tornado's track speed, denoted by the red curve $C_{tro}(t)$ in Fig. 7c, varied slightly along the red dotted loop (Fig. 7b). $C_{tro}(t)$ sped up and slowed down; $Dir_{tro}(t)$ varied nonlinearly as the tornado rotated cyclonically and periodically around the mesocyclone center. The difference between the minimum and maximum values of $C_{tro}(t)$ is 10 m s^{-1}. At the same time, the tornado's translational direction $Dir_{sv}(t)$ changed linearly (orange curve).

3.4 Experiment D

In the last few subsections, we discussed the effects of the $C_{sv\_\tau}(t)$-to-$C_{pv}(t)$ ratios on the transient behaviors of simulated tracks. We now investigate the effects of linear increase in $C_{pv}(t)$ on the behaviors of the tracks, while other parameters remain fixed. To simulate a varying parent mesocyclone speed, $C_{pv}(t)$ may be analytically expressed as

$$C_{pv}(t) = C_{pv}(t_b) + [C_{pv}(t_e) - C_{pv}(t_b)]\left(\frac{t-t_b}{t_e-t_b}\right) \ , \quad (21a)$$

$$\frac{dC_{pv}(t)}{dt} = \frac{C_{pv}(t_e)-C_{pv}(t_b)}{t_e-t_b} \ , \quad (21b)$$

where $C_{pv}(t_b)$ is assumed to be 1 m s^{-1} at $t_b = 0$ and $C_{pv}(t_e)$ is assumed to be 40 m s^{-1} at $t_e = 30$ min (Table 1). This represents a linear, rapid increase in the mesocyclone's vortex movement speed. Eq. (21b) is a constant acceleration that the mesocyclone experiences in a rectilinear motion.

Figure 8 presents the effects of varying mesocyclone's translational speed on the tornado's trochoidal speed and direction. Between 0 and 11 min, a "tilted" loop was produced with decreasing $R > 1.0 = R_{cyc}$. Note that this tilted loop is not shown in Fig. 1, because $C_{pv}(t)$ is constant in the figure. Comparing to the upright loop (red, vertical line passing through the center of the first loop in Fig. 7a), the loop was tilted backward owing to the increased-propagating mesocyclone. As $C_{pv}(t)$ increased linearly, the trochoidal marks transformed from once-executed loop to broadly-peaked ridges and flatter troughs. The $C_{tro}(t)$ curve was amplified, corresponding to the linear increase of $C_{pv}(t)$. The "tilted" loops have been observed in Fig. 83 of Fujita et al. (1970) and Fig. 21 of Agee et al. (1977). The second slightly tilted loop associated with the El Reno, Oklahoma tornado near 2325 UTC is shown in Fig. 2.

3.5 Experiment E

Previously, the linear increase in $C_{pv}(t)$ changed the $C_{sv\_\tau}(t)$-to-$C_{pv}(t)$ ratios which, in turn, impacted the transient behaviors of simulated tracks including the backward tilted loop. Now, we reverse Experiment D by stating that in Eq. (21), $C_{pv}(t_b)$ is now 40 m s^{-1} at t_b = 0 min and $C_{pv}(t_e)$ is now 1 m s^{-1} at t_e = 30 min (Table 1). This reverse represents a linear, rapid decrease in the translational speed of the mesocyclone.

Figure 9 is very similar to Fig. 8, except that the former figure was a mirror image of the latter figure. This image was a reflected duplication of evolutionary characteristics that appeared almost identical but were reversed.

3.6 Experiment F

In the last five experiments, we demonstrated how the effects of varying $C_{pv}(t)$ impact the evolutionary characteristics of the tornado's trochoidal motion, while other parameters remained unchanged including the constant $\Omega_{sv}(t)$, as shown in Table 1. Now, we begin to explore the role of varying $\Omega_{sv}(t)$ in influencing the complex trochoidal/cycloidal/looping tracks. Analogous to the development of Eq. (21), $\Omega_{sv}(t)$ may be analytically given by

$$\Omega_{sv}(t) = \Omega_{sv}(t_b) + [\Omega_{sv}(t_e) - \Omega_{sv}(t_b)]\left(\frac{t-t_b}{t_e-t_b}\right) \ , \quad (22a)$$

$$\frac{d\Omega_{sv}(t)}{dt} = \frac{\Omega_{sv}(t_e)-\Omega_{sv}(t_b)}{t_e-t_b} \ , \quad (22b)$$

where $\Omega_{sv}(t_b)$ is assumed to be 3.33×10^{-3} s^{-1} at $t_b = 0$ min and $\Omega_{sv}(t_e)$ is assumed to be 2.0×10^{-2} s^{-1} at $t_e = 30$ min. Eq. (22) shows the linear increase of $C_{sv}(t)$ from 5 to 55 m s^{-1}. Other parameters, including the constant $C_{pv}(t)$ value of 25 m s^{-1}, remain unchanged (Table 1).

As R increases linearly and progressively in Fig. 10, the trochoidal marks transform from the broadly-peaked track, through a cycloidal track with a zero-angle cusp, to a few loops. While a propagating mesocyclone traveled eastward at a constant $C_{pv}(t)$, the tornado center rapidly and cyclonically revolved around the mesocyclone center at the progressively increased revolution speeds $C_{sv}(t)$ of the tornado. The varying $C_{sv}(t)$ caused to (a) change trochoidal marks and motions, (b) increase the distance between two successive red dots along the red dotted path, (c) decrease the distance between the two consecutive points of zero slope, and (c) increase the loop size. The highly nonlinear $C_{tro}(t)$ curve amplifies increasingly, corresponding to the linear increased $\Omega_{sv}(t)$ and $C_{sv}(t)$.

4. CONCLUSIONS AND FUTURE WORK

A model of subvortex trochoidal motion in which parametric equations were developed to investigate and interpret the transient behaviors of simulated trochoidal tracks traced out by a hypothetical subvortex (tornado) revolving around a hypothetical parent vortex (mesocyclone) was presented. The evolutionary characteristics of several parameters were produced by plotting time series to elucidate such behaviors that bear resemblance to the observed tornado damage tracks during tornado revolution around a parent mesocyclone (e.g., Fig. 2). The trochoidal motion of the subvortex depends heavily upon (a) the rectilinear/curvilinear motion of the parent vortex, (b) the radial distance from the parent vortex axis to the subvortex axis, (c) the angular velocity at which the subvortex revolves around the parent vortex, and (d) the ratio of the subvortex's revolution speed to the parent vortex's translational speed. Although trochoidal marks are the most interesting and useful of the marks left by tornadoes crossing open fields and towns (Fig. 2), we believe that the model developed in this study highlights the gap in our current understanding and interpretation of the relationship between the trochoidal motion simulations and the observed tornado damage tracks.

In our on-going work, we plan to demonstrate that a model multiple-vortex tornado revolving around a model parent mesocyclone will produce trochoidal marks traced out by the model multiple-vortex axes rotating cyclonically around the model parent tornado axis. In the near future, we plan to map out near-surface tornadic wind fields produced by an analytical or numerical tornado revolving around an analytical or numerical parent mesocyclone in an attempt to determine the duration of ground-relative wind speeds along a rectilinear/curvilinear tornado damage track. The duration patterns may be used to assess and interpret the EF damage intensity isopleths.

The parent mesocyclone motion [i.e., $C_{pv}(t)$ and $Dir_{pv}(t)$] and path length (i.e., PL_{pv}), the tornado's radial distance [i.e., $D_{sv}(t)$] from the mesocyclone axis, and the tornado's angular velocity [i.e., $\Omega_{sv}(t)$] are the most important parameters that can be estimated from successive volume scans of Doppler radar data at lowest elevation angles. The estimated parameters enable the tornado's trochoidal motion and damage path length to be computed.

In our near-future works, the trochoidal motion model will be applied to our phased-array radar simulation studies. The simulation will produce single-Doppler data by scanning across a model tornado that revolves cyclonically around a model parent mesocyclonic circulation at proximity to the radar site. Zrnić and Istok (1980) provided single-Doppler data suggesting that the Del City, Oklahoma tornado of 20 May 1977 was revolving cyclonically about a parent mesocyclonic circulation located at 35-40 km from the National Severe Storms Laboratory (NSSL) Doppler radar. As stated by Wakimoto et al. (2003), no visual information on the funnel or detailed damage survey was provided to confirm this trochoidal motion.

Acknowledgments. The author thanks Terry Schuur and Rodger Brown of NSSL for providing helpful comments that lead to improvement of the manuscript. Roger Edwards of NOAA NWS Storm Prediction Center and Doug Speheger of NOAA NWSWFO in Norman, OK provided inspiring discussion.

5. REFERENCES

Agee, E. M., J. T. Snow, and P. R. Clare, 1976: Multiple vortex features in the tornado cyclone and the occurrence of tornado families. *Mon. Wea. Rev.,* **104**, 552-563, doi:10.1175/1520-0493(1976)1042.0.CO;2.

Agee, E. M., J. T. Snow, F. S. Nickerson, P. R. Clarke, C. R. Church, and L. A. Schaal, 1977: An observational study of the West Lafayette, Indiana, tornado of 20 March 1976. *Mon. Wea. Rev.,* **105**, 893-907.

Atkins, N. T., K. M. Butler, K. R. Flynn, and R. M. Wakimoto, 2014: An integrated damage, visual, and radar analysis of the 2013 Moore, Oklahoma, EF5 tornado. *Bull. Amer. Meteor. Soc.,* **95**, 1549-1561, doi:10.1175/BAMS-D-14-00033.1.

Bluestein, H. B., 1983: Surface meteorological observations in severe thunderstorms: Part II: Field experiments with TOTO. *J. Climate Appl. Meteor.,* **22**, 919-930.

Brown, J. M., and K. R. Knupp, 1980: The Iowa cyclonic-anticyclonic tornado pair and its parent thunderstorm. *Mon. Wea. Rev.,* **124**, 384-407, doi:10.1175/1520-0493(1980)1082.0.CO;2.

Brown, R. A., L. R. Lemon, and D. W. Burgess, 1978: Tornado detection by pulsed Doppler radar. *Mon. Wea. Rev.,* **106**, 29-38.

Burgess, D., K. Ortega, G. Stumpf, G. Garfield, C. Karstens, T. Meyer, and B. Smith, 2014: 20 May 2013 Moore, Oklahoma, tornado: Damage survey and analysis. *Wea. Forecasting*, **29**, 1229-1237.

Forbes, G. S., and H. B. Bluestein, 2001: Tornadoes, tornadic thunderstorms, and photogrammetry: A review of the contributions by T. T. Fujita. *Bull. Amer. Meteor.,* **82**, 73-96.

French, M. M., H. B. Bluestein, I. PopStefanija, C. A. Baldi, R. T. Bluth, 2014: Mobile, phased-array, Doppler radar observations of tornadoes at X band. *Mon. Wea. Rev.,* **143**, 1010-1036, doi: 10.1175/MWR-D-13-00101.1.

Fujita, T. T., 1963: Analytical mesometeorology: A review. *Severe Local Storms, Meteor. Monogr.,* No. 27, Amer. Meteor. Soc., 77-125.

Fujita, T. T., 1981: Tornadoes and downburst in the context of generalized planetary scales. *J. Atmos. Sci.,* **38**, 1511-1534, doi:10.1175/1520-0469(1981)0382.0.CO;2.

Fujita, T. T., D. L. Bradbury, and C. F. van Thullenar, 1970: Palm Sunday tornadoes of April 11, 1965. *Mon. Wea. Rev.,* **98**, 29-69, doi:10.1175/1520-0493(1970)0982.3.CO;2.

Heinselman, P. L., D. L. Priegnitz, K. L. Manross, T. M. Smith, and R. W. Adams, 2008: Rapid sampling of severe storms by the National Weather Radar Testbed phased array radar. *Wea. Forecasting,* **23,** 808-824, doi:10.1175/2008WAF-D2007071.1.

Kurdzo, J. M., D. J. Bodine, B. L. Cheong, and R. D. Palmer, 2015: High-temporal resolution polarimetric X-band Doppler radar observations of the 20 May 2013 Moore, Oklahoma, tornado. *Mon. Wea. Rev.,* **143**, 2711-2735, doi:10.1175/MWR-D-14-00357.1.

Ray, P. S., C. E. Hane, R. P. Davies-Jones, and R. L. Alberty, 1976: Tornado-parent storm relationship deduced from a dual-Doppler radar analysis. *Geophys. Res. Lett.,* **3**, 721-723.

Wakimoto, R. M., and N. T. Atkins, 1996: Observations on the origins of rotation: The Newcastle tornado during VORTEX 94. *Mon. Wea. Rev.,* **124**, 384-407.

Wakimoto, R. M., H. V. Murphey, D. C. Dowell, and H. B. Bluestein, 2003: The Kellerville tornado during VORTEX: Damage survey and Doppler radar analyses. *Mon. Wea. Rev.,* **131**, 2197-2221, doi:10.1175/1520-0493(2003)1312.0.CO;2.

Wakimoto, R. M., N. T. Atkins, K. M. Butler, H. B. Bluestein, K. Thiem, J. Snyder, and J. Houser, 2015: Photogrammetric analysis of the 2013 El Reno tornado combined with mobile X-band polarimetric radar data. *Mon. Wea. Rev.,* **143**, 2657-2683, doi:10.1175/MWR-D-15-0034.1.

Wakimoto, R. M., N. T. Atkins, K. M. Butler, H. B. Bluestein, K. Thiem, J. C. Snyder, J. Houser, K. Kosiba, and J. Wurman, 2016: Aerial damage survey of the 2013 El Reno tornado combined with mobile radar data. *Mon. Wea. Rev.,* **144**, 1749-1776, doi:10.1175/MWR-D-15-0367.1.

Wurman, J., and S. Gill, 2000: Finescale radar observations of the Dimmitt, Texas (2 June 1995), tornado. *Mon. Wea. Rev.,* **128**, 2135-2164, doi:. http://dx.doi.org/10.1175/15200493(2000)128<2135:FROOTD>2.0.CO;2

Wurman, J., K. Kosiba, P. Robinson, and T. Marshall, 2013: The role of multiple-vortex tornado structure in causing storm researcher fatalities. *Bull. Amer. Meteor. Soc.,* **95**, 31-45, doi:10.1175/BAMS-D-13-00221.1.

Zrnić, D., and M. Istok, 1980: Wind speeds in two tornadic storms and a tornado deduced from Doppler spectra. *J. Appl. Meteor.,* **19**, 1405-1415.

TABLE 1. Initial parameters that generate trochoidal tracks traced out by a model tornado axis revolving around a model parent mesocyclone axis as a function of time (t) up to 30 min are presented for six experiments (EXP) A-F. An arrow (→) located between two values represents a transient change from one value at $t = t_o$ to another value at $t = t_o + \Delta t$, where Δt = 10 s. Units are: $C_{pv}(t)$ in m s^{-1}; $Dir_{pv}(t)$ in deg; $\theta_{pv}(t)$ in deg; $D_{sv}(t)$ in km; $\Omega_{sv}(t)$ in s^{-1}; $C_{sv\_t}(t)$ in m s^{-1}; and θ_{sv} in deg.

	Mesocyclone			Tornado			
EXP	$C_{pv}(t)$	$Dir_{pv}(t)$	$\theta_{pv}(t)$	$D_{sv}(t)$	$\Omega_{sv}(t)$	$C_{sv\_\tau}(t)$	θ_{sv}
A	*25*	*90º*	*0º*	*1.5*	*10^{-2}*	*15*	*270º*
B	*15*	*90º*	*0º*	*1.5*	*10^{-2}*	*15*	*270º*
C	*5*	*90º*	*0º*	*1.5*	*10^{-2}*	*15*	*270º*
D	*1→40*	*90º*	*0º*	*1.5*	*10^{-2}*	*15*	*270º*
E	*40→1*	*90º*	*0º*	*1.5*	*10^{-2}*	*15*	*315º*
F	*25*	*90º*	*0º*	*1.5*	*0.0033→0.02*	*5→55*	*0º*

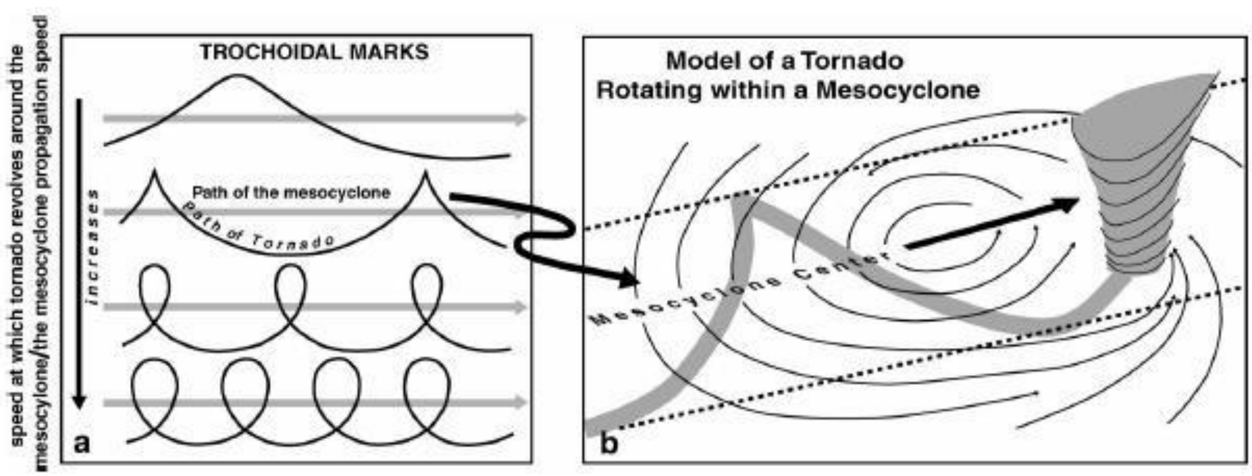

FIG. 1. Idealized illustration of (a) basic trochoidal marks (black curves) as a function of a hypothetical tornado center's rotational speed around a hypothetical mesocyclone center (gray arrows) and the motion of the mesocyclone and (b) a tornado track (gray shaded curve) if the ratio of the tornado's rotational speed to the mesocyclone's vortex movement speed is equal to one. [Figure from Wakimoto et al. (2003)].

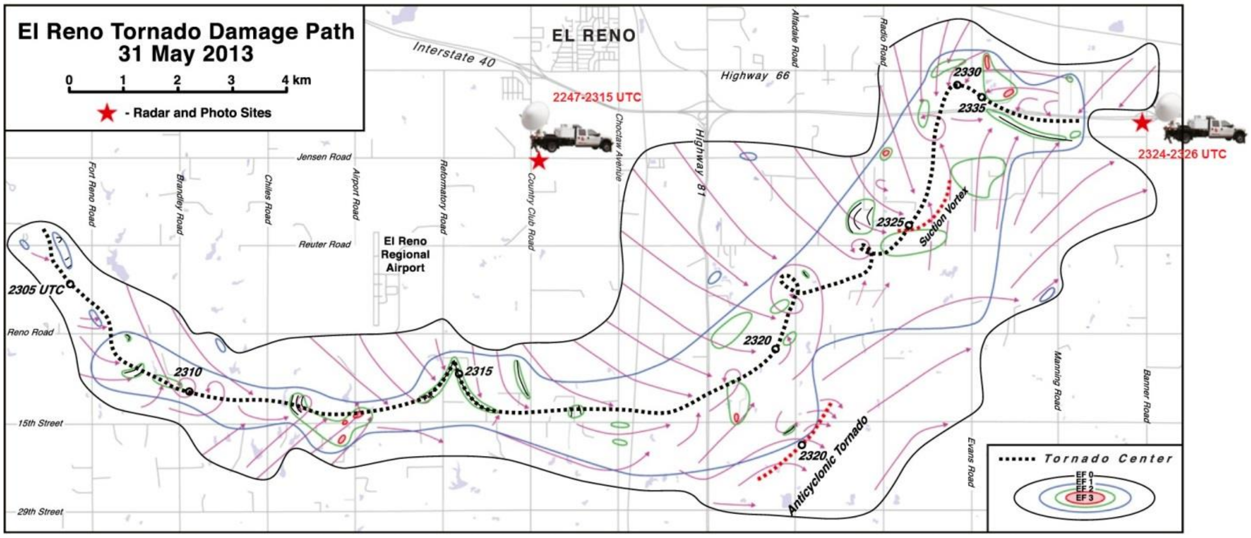

FIG. 2. Damage map of the El Reno, OK tornado of 31 May 2013. Black, blue, green, and red contours, respectively, denote the EF0, -1, -2, and -3 damage intensity isopleths. The tornado's path, including loops and cusps, is indicated by a black, dotted curve; Black, thick circles denote the time (UTC) of the radar-indicated location of the tornado. Two red, dotted curves denote the location of an anticyclonic tornado and cyclonic suction vortex. Magenta arrows represent the approximate flow depicted in the damage based on fallen trees, building debris, and streaks in the vegetation based on a detailed aerial survey. Red stars denote two deployment locations and times of the RaXPol mobile Doppler radar (shown by an icon of the truck). Photographs and high-definition video of the tornado were taken at both sides. [Figure from Wakimoto et al. (2015, 2016)].

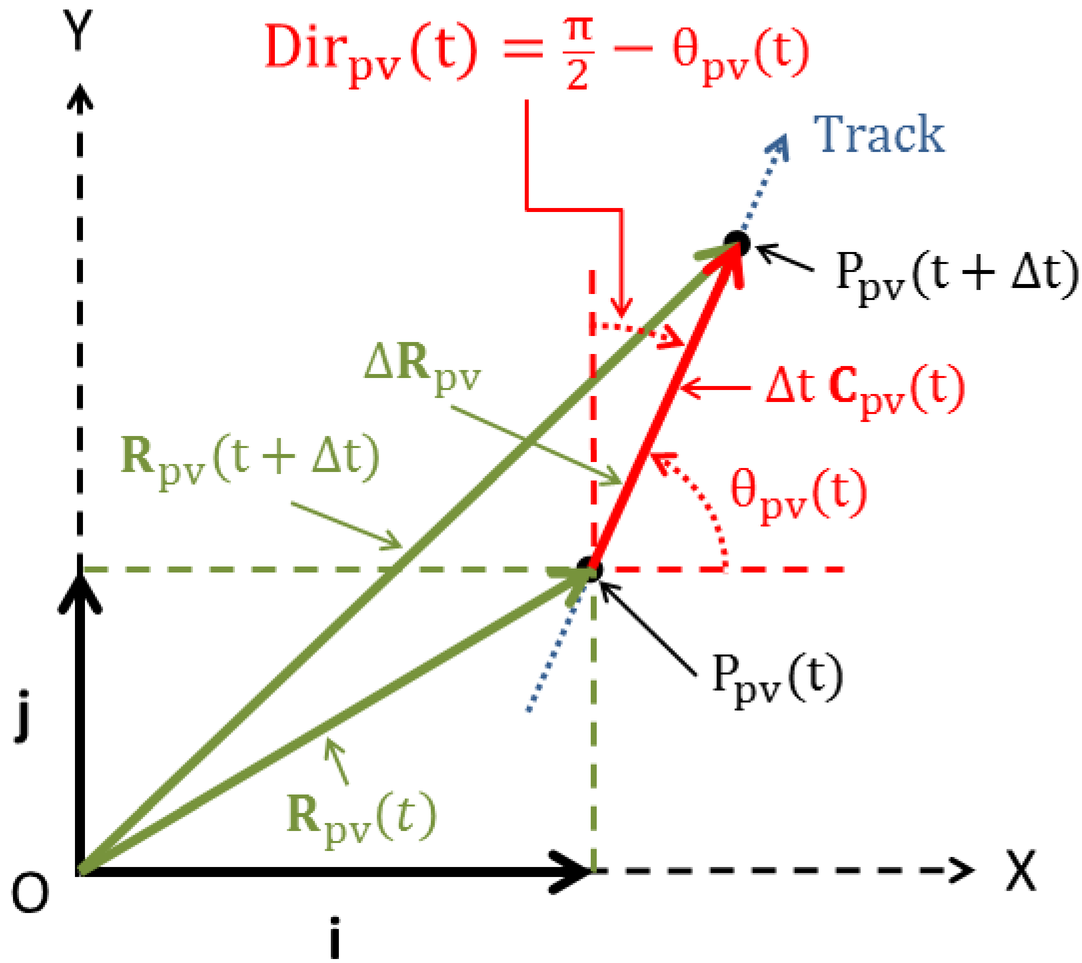

FIG. 3. Positions of a parent vortex axis P_{pv} at two different times t and $t+\Delta t$, relative to a given reference frame with origin O, are given by the parent vortex position vectors $\boldsymbol{R}_{pv}(t)$ and $\boldsymbol{R}_{pv}(t+\Delta t)$ (green arrows) from point O to points $P_{pv}(t)$ and $P_{pv}(t+\Delta t)$ (heavy black dots). The initial translational direction $\theta_{pv}(t)$ at $t=0$ between the parent vortex track angle and the x-axis is measured counterclockwise from due east. The unit vectors, denoted by $\boldsymbol{i}$ and $\boldsymbol{j}$, are parallel to the x- and y-axes, respectively. A blue circle with two arrows within which P_{pv} is centered represents a cyclonically rotating parent vortex. Δt is a small increment of time. The parent vortex moving at its (red) vector velocity $\boldsymbol{C}_{pv}(t)$ along a path (track) is indicated by a blue dotted line.

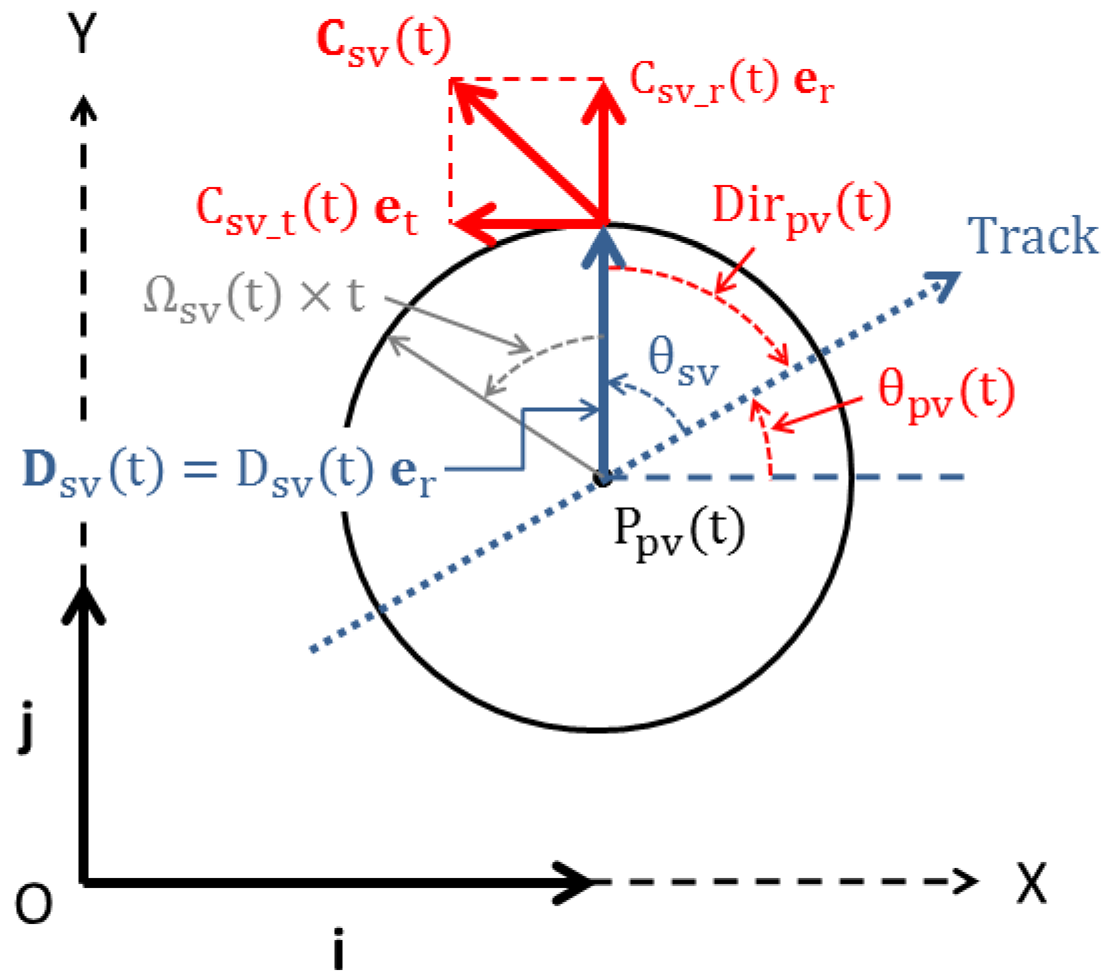

FIG. 4. Idealized illustration of the motion of a subvortex in a circular trajectory having $\Omega_{sv}(t)$. The radial and tangential components of the subvortex motion (speed and vortex movement direction) on the circumference of a circle (black) having its radius $D_{sv}(t)$ (blue thick line) are, respectively, indicated by the stretching (or shrinking) position vector $C_{sv\_r}(t)\ \mathbf{e}_r$ and the rotational velocity vector $C_{sv\_t}(t)\ \mathbf{e}_t$ relative to the position of the parent vortex point $P_{pv}(t)$. A blue, dotted line represents a track of the parent vortex.

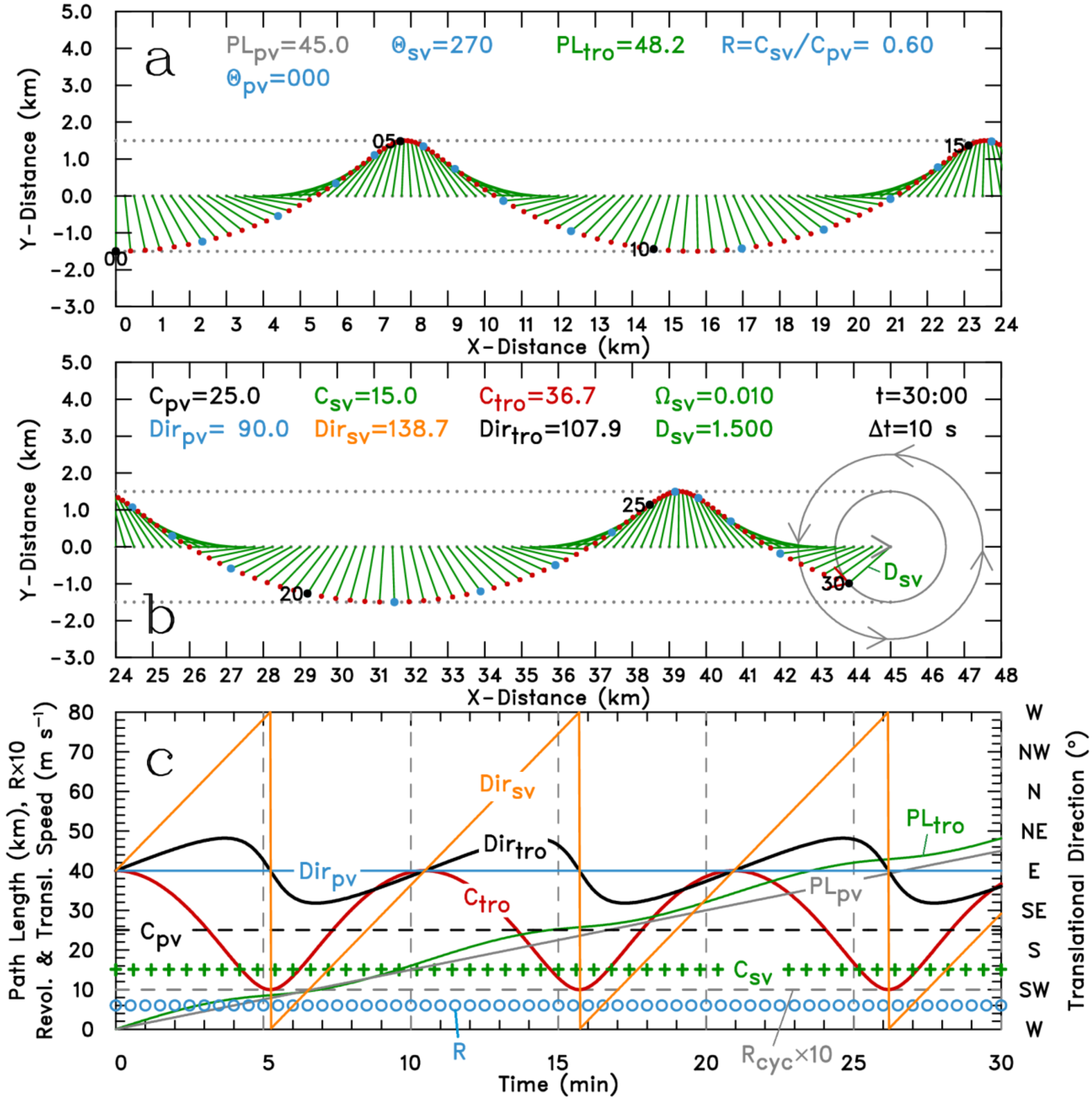

FIG. 5. Experiment A: (a)-(b) A simulated trochoidal track (red dotted curve) traced out by a simulated tornado (gray inner circle) revolving around a simulated parent mesocyclone (gray outer circle with four arrowheads) moving toward east (Dir_{pv} = 90º) at C_{pv} = 25 m s^{-1} as a function of time (t, mm:ss). Δt is the time increment (10 s) between two red dots. One blue (black) dot on the red dotted curve represents a phased-array (WSR-88D) radar's updates of one minute (5 min). (c) The evolutionary characteristics of C_{pv} (m s^{-1}, black dashed line), C_{sv} (m s^{-1}, green plus line), C_{tro} (m s^{-1}; red solid curve), Dir_{pv} (º; blue line), Dir_{tro} (º, black solid curve), Dir_{sv} (º, orange curve), $R \times 10$ (blue circled curve), PL_{tro} (km, green solid curve), and PL_{pv} (km, gray solid curve) are indicated. Note that on the left-hand side of the panel where $R \times 10$ is labelled to avoid overcrowding with other profiles. The labelled $R_{cyc} \times 10$ is indicated by a gray horizontal dashed line that represents the line at which a cycloid occurs at $R_{cyc} = 1.0$. A vertical dashed line represents time (min) corresponding to the time of the trochoidal track position (black dot on red dotted curve). A tick mark along the abscissa represents a one-minute apart. In panel b, the values of C_{pv}, C_{sv}, C_{tro}, Dir_{pv}, Dir_{tro}, Dir_{sv}, R, PL_{tro},and PL_{pv} vary with time at the last point of the trochoidal track (red arrow at the end of the red dotted curve). Click [here]() for trochoidal motion animation.

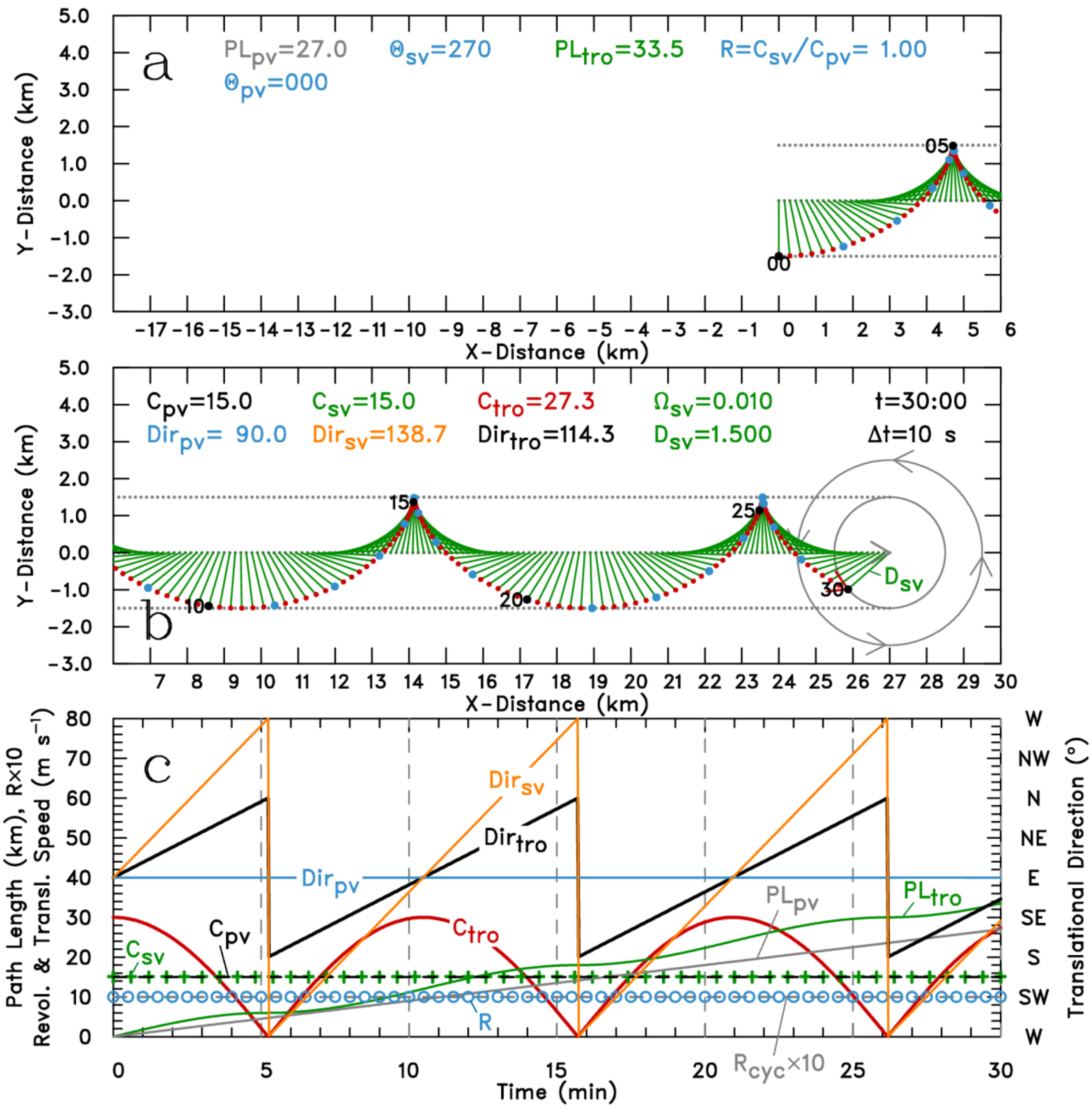

FIG. 6. Experiment B: Same as FIG. 5, except that C_{pv} decreases to 15 m s^{-1} to match C_{sv} . Click here for trochoidal motion animation.

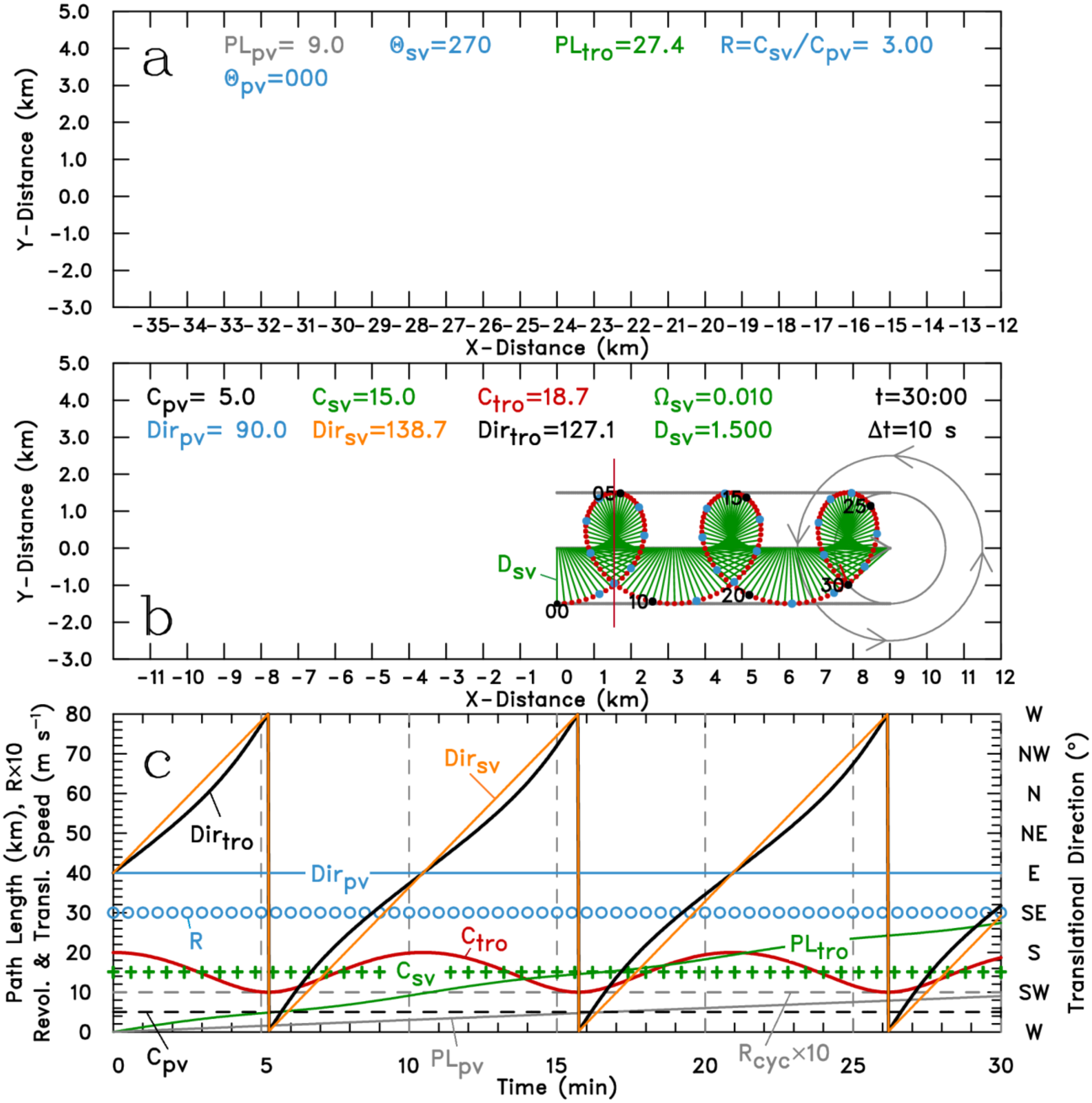

FIG. 7. Experiment C: Same as FIG. 5, except that C_{pv} decreases to 5 m s^{-1} to be less than C_{sv}. In (a), a red, vertical line is discussed in text for comparing to that in FIGS. 8 and 9. Click here for trochoidal motion animation.

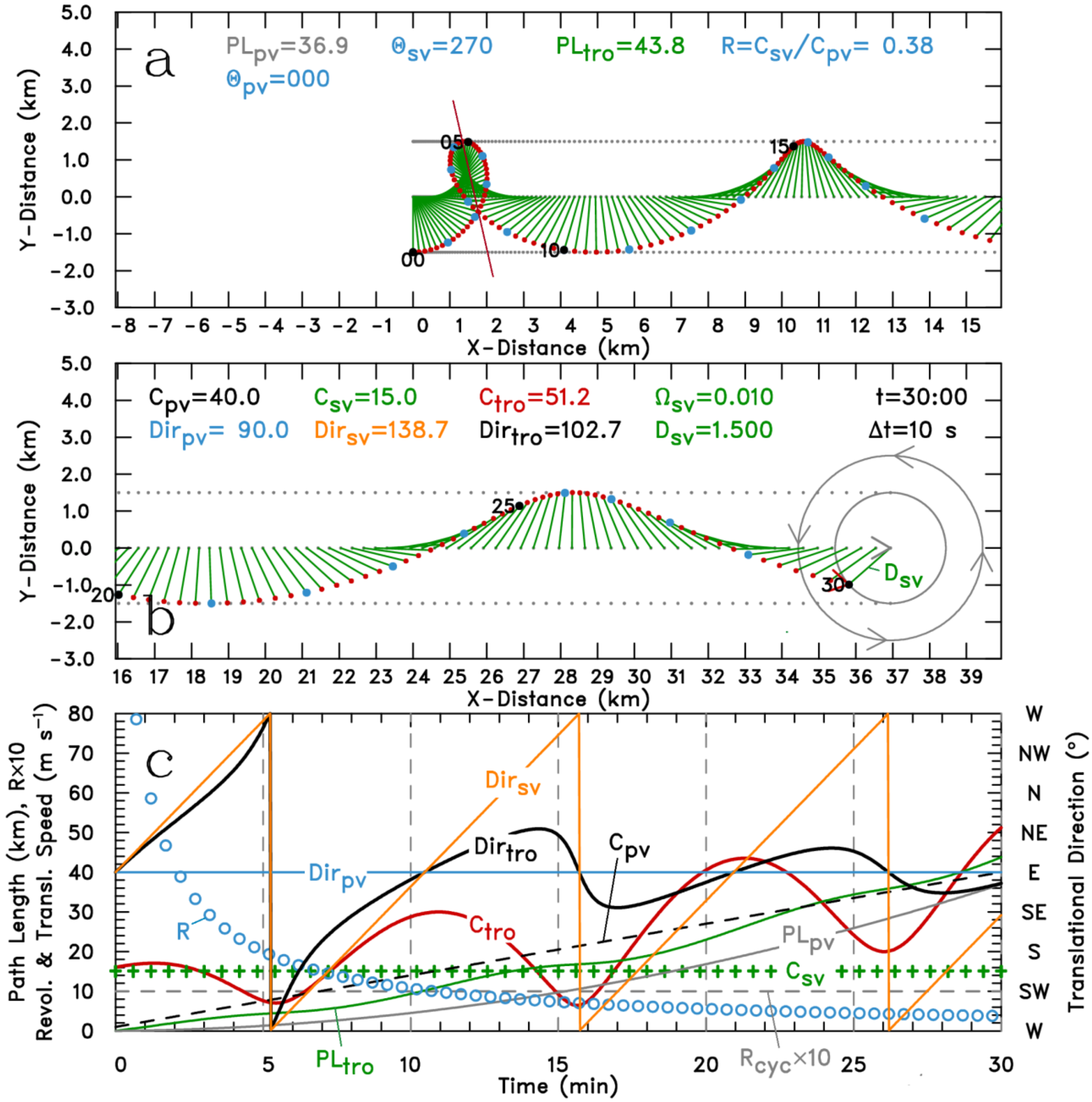

FIG. 8. Experiment D: Same as FIG. 5, except that C_{pv} linearly accelerates from 1 m s^{-1} at $t_b = 0$ to 40 m s^{-1} at $t_e =$ 30 min. In panel b, a red sloping line is described in text. Click [here]() for trochoidal motion animation.

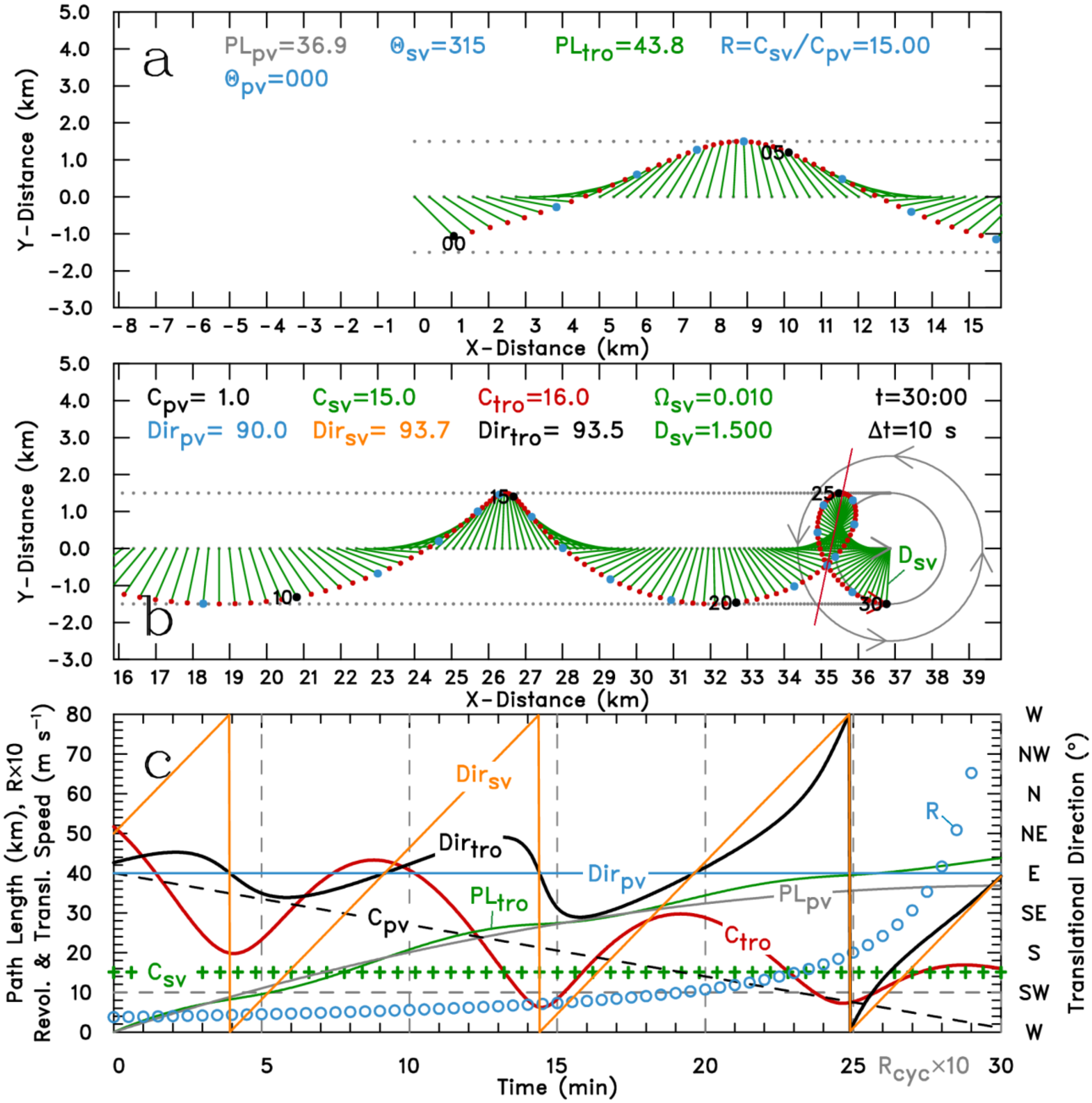

FIG. 9. Experiment E: Same as FIG. 8, except that C_{pv} linearly decelerates from 40 m s^{-1} at t_b = 0 to 1 m s^{-1} at t_e = 30 min. Click [here](#) for trochoidal motion animation.

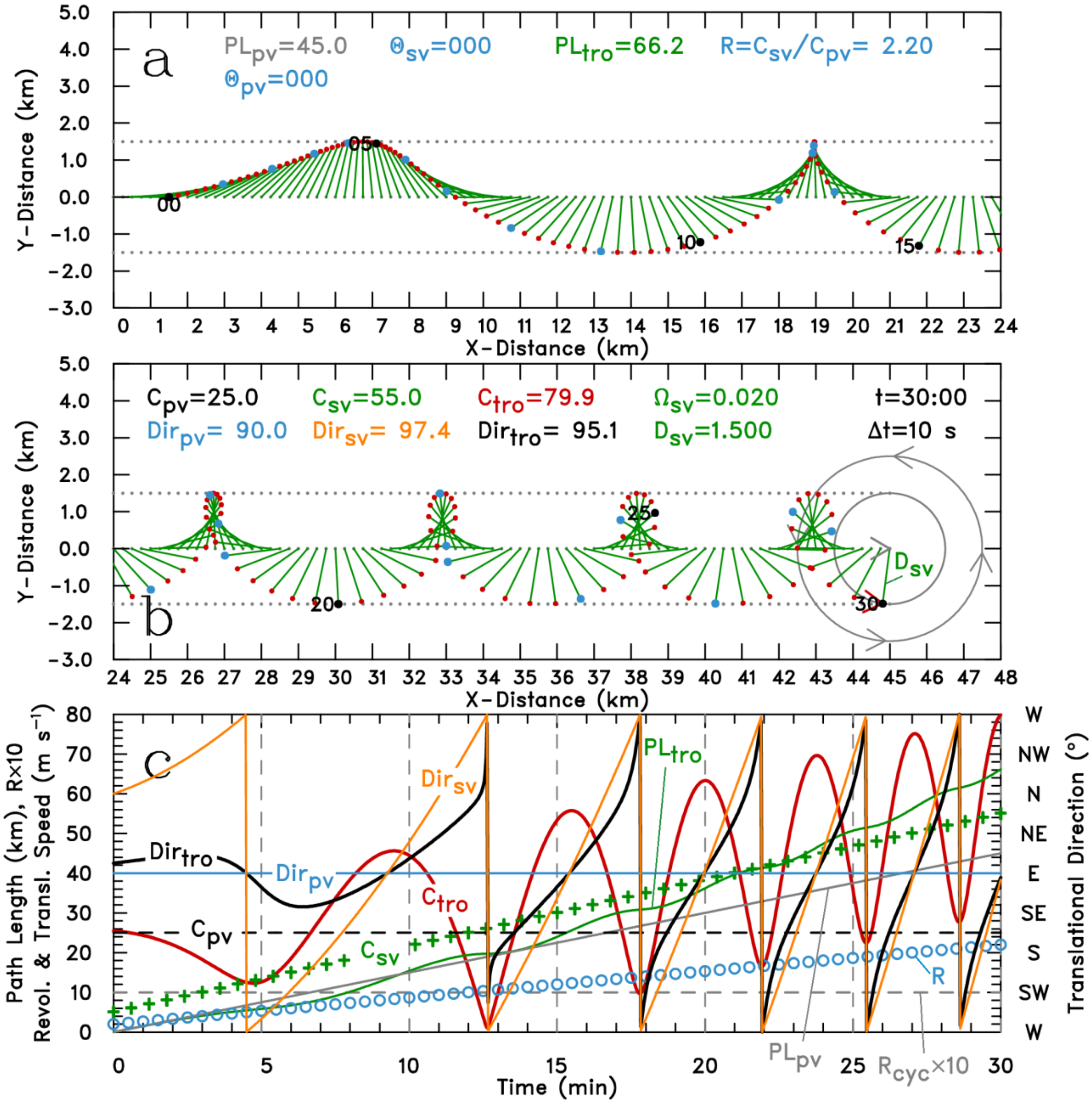

FIG. 10. Experiment F: Same as FIG. 5, except that C_{sv} linearly accelerates from 5 m s^{-1} at t_b = 0 min to 55 m s^{-1} at t_e = 30 min. Click [here](#) for trochoidal motion animation.